COMMUNICATION

Inexpensive Hole Transporting Materials Derived from Tröger's Base Afford Efficient and Stable Perovskite Solar Cells

Titas Braukyla,†[a] Rui Xia,†[b] Maryte Daskeviciene,[a] Tadas Malinauskas,[a] Alytis Gruodis,[c] Vygintas Jankauskas,[c] Zhaofu Fei,[d] Cristina Momblona,[b] Cristina Roldán-Carmona,[b] Paul J. Dyson,[d] Vytautas Getautis,*[a] Mohammad Khaja Nazeeruddin*[b]

[a] Department of Organic Chemistry, Kaunas University of Technology, Radvilenu pl. 19, 50254, Kaunas, Lithuania
[b] Group for Molecular Engineering of Functional Materials, Institute of Chemical Sciences and Engineering, École Polytechnique Fédérale de Lausanne, Rue de l'Industry 17, CH-1951, Sion, Switzerland
[c] Institute of Chemical Physics Vilnius University, Sauletekio al.3, Vilnius LT-10257, Lithuania
[d] Institut des Sciences et Ingénierie Chimiques, Ecole Polytechnique Fédérale de Lausanne (EPFL), CH - 1015 Lausanne, Switzerland
† T. B. and R. X. contributed equally to this work

Abstract: We report the synthesis of three novel enamine hole-transporting materials (HTMs) based on Tröger's base scaffold. These compounds are obtained in a three-step facile synthesis from commercially available materials, without the need of expensive catalysts, inert conditions or time consuming purification steps. The best performing material, HTM3, demonstrated 18.62 % PCE in PSCs, rivaling Spiro-OMeTAD in efficiency, and showing markedly superior long-term stability in non-encapsulated devices. In dopant-free PSCs HTM3 outperformed Spiro-OMeTAD by 1.6 times. The high glass transition temperature (Tg = 176 °C) of HTM3 also suggests promising perspectives in device applications.

Perovskite solar cells (PSCs) are promising affordable candidates for efficient harvesting of abundant solar energy. PSCs represent the most significant breakthrough in photovoltaic technology since the 1990s, with an increase in their power conversion efficiency (PCE) from less than 5% to over 23% in just a few years [1–3]. Their remarkable performances can be attributed to excellent optoelectronic properties, such as high absorption coefficient [4,5], low exciting binding energy [6], high conductivity and charge carrier mobility [7–9], and long carrier diffusion length [10,11]. Until now, most of the high efficiency PSCs are based on either the small organic molecule 2,2`,7,7`-tetrakis(*N*,*N*-di-*p*-methoxy-phenylamine)-9,9`-spirobifluorene (Spiro-OMeTAD) or conjugated macromolecule poly[bis(4-phenyl)(2,4,6-trimethylphenyl)amine] (PTAA) hole-transporting materials (HTMs), both of which are expensive [12,13]. Their high cost, due to complex multi-step synthesis and costly purification procedures, is therefore a limiting factor for the realization of cost-effective and stable devices [8,14]. To engineer cheaper HTMs, shorter reaction schemes with simple purification procedures are required. Successful examples include branched methoxydiphenylamine substituted fluorine [15] and bifluorenylidene-based derivatives [16], spiro[fluorene-9,9`-xanthene]-based materials [17–19] and methoxydiphenylamine substituted branched carbazole derivatives [20–22]. Nevertheless, these molecules[15,18] are synthesized via cross-coupling reactions that require transition metal catalysts, inert reaction conditions, and extensive product purification in order to remove catalyst residue, which in turn increases cost of the final product.

Recently, we reported a simple carbazole-based conjugated enamine named V950 via an extremely simple synthetic route. This new small-molecule was prepared in one-step without the use of expensive catalysts, column chromatography or sublimation steps, resulting in a material rivaling Spiro-OMeTAD [23]. Moreover, Tröger's base (TB) can serve as a functional core, allowing the synthesis of materials which exhibit HTM properties and high charge mobility [24]. They have an easily obtainable core,

providing non-planar orientation for substituents and structural branches towards each other. Thus, expanding its structure *via* enamine condensation can increase both structural bulk and expand conjugated π systems multiple times, providing easily obtainable, cheap and efficient HTMs.

Here we describe the synthesis and application of V-shaped TB derivatives **HTM1**–**HTM3** (Figure 1) bearing enamine-linked diphenyl branches. These materials can be obtained without palladium catalyzed reactions or costly purification techniques, affording cheap, high-performance HTMs. Moreover, we can avoid column chromatography or vacuum sublimation processes for the purification of **HTM3**, which is thermally stable, solution processable, has a high hole-drift mobility and leads to PCEs > 18.5 %.

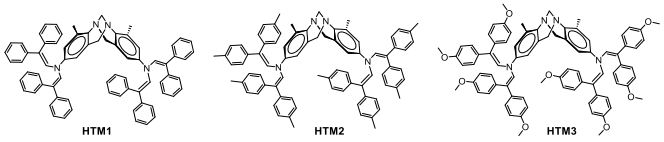

Figure 1. Structures of **HTM1**–**HTM3**.

Novel TB enamines N^2,N^2,N^8,N^8-tetrakis(2,2-diphenylethenyl)-4,10-dimethyl-6*H*,12*H*-5,11-methanodibenzo[*b*,*f*][1,5]diazocine-2,8-diamine (**HTM1**), N^2,N^2,N^8,N^8-tetrakis[2,2-bis(4-methylphenyl)ethenyl]-4,10-dimethyl-6*H*,12*H*-5,11-methanodibenzo[*b*,*f*][1,5]diazocine-2,8-diamine (**HTM2**), and N^2,N^2,N^8,N^8-tetrakis[2,2-bis(4-methoxyphenyl)ethenyl]-4,10-dimethyl-6*H*,12*H*-5,11-methanodibenzo[*b*,*f*][1,5]diazocine-2,8-diamine (**HTM3**) were synthesized *via* intermediate TB compounds **1** and **2** (Scheme 1**Error! Reference source not found.**). Initially, nitro groups containing TB **1** were obtained from 2-methyl-4-nitroaniline and paraformaldehyde in trifluoroacetic acid. Reduction of the nitro groups in **1** is achieved under reflux with iron powder suspended in a mixture of acetic acid and ethanol, affording diamino derivative **2**. Finally, enamines **HTM1**–**HTM3** were obtained by reaction of **2** and the corresponding aldehyde (diphenyl-, bis(4-methylphenyl)-, or bis(4-methoxyphenyl)-acetaldehyde) in THF under reflux in the presence of (+/-)-camphor-10-sulfonic acid (CSA).

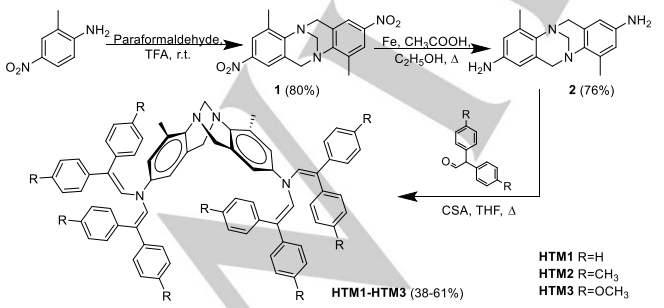

Scheme 1. Synthesis of Tröger's base compounds **HTM1**–**HTM3**.

The structures of **HTM1**–**HTM3** were confirmed by ^{1}H and ^{13}C NMR spectroscopy as well as elemental analysis. The signals in the ^{1}H NMR spectra in the region 3.6-4.5 ppm confirms the methanodiazocine bridge, and hence the presence of the TB core (Figures S10, S12, S14). For example, in the ^{1}H NMR spectrum of **HTM2** (Figure S12) the bridging methylene protons (Ar-CH_2-N) show two doublets at 4.45 and 3.97 ppm, i.e. *endo* and *exo* hydrogens respectively, as these protons are magnetically nonequivalent due to the TB rigid structure. The singlet for the two protons of the other bridging methylene carbon (N-CH_2-N) is observed at 4.20 ppm, while those for CH-N protons of the enamine groups are observed at 5.77-5.56 ppm. Interestingly, the proton signals of the terminal methoxy groups are split in two singlets at 3.67 and 3.81 ppm (Figure S14), indicating that due to molecular configuration they become energetically unequal. Notably, final **HTM2** and **HTM3**, bearing methyl or methoxy groups on each terminal phenyl ring, are soluble in common organic solvents such as THF, chloroform, toluene, or chlorobenzene, typically used in PSCs.

To assess the cost-effectiveness of the HTMs, we performed material cost estimations for the synthesis of **HTM3** based on the procedure established by Osedach et al. (Table S3, Supporting Information) [25]. The estimated material cost is ≈10 \$ g^{-1} which is less than 1/9 of the cost of spiro-OMeTAD (≈92 \$ g^{-1}) [26]. Furthermore, this material does not require expensive palladium-catalyzed cross coupling reactions, sublimation or column chromatography purification procedures, avoiding the presence of organic impurities and catalyst residues acting as charge carrier traps or photoquenchers[16,27,28]. Moreover, omitting column chromatography purification step also saves significant amount of solvents, therefore not only the **HTM3** production cost is lower**,** but so is the impact on the environment.

To gain insights into the molecular structure, quantum chemical calculations of **HTM1**–**HTM3** were performed using the Gaussian 09 software [29]. Optimized molecular structures of V-shaped compounds **HTM1**–**HTM3** (after ground state geometry optimization) in XY and XZ projections are presented in Supplementary Information, Figure S01. The structure is based on a "molecular tweezer", consisting of the central TB fragment, its two aromatic planes forming an angle that exceeds 105°, and fragments of enamine-linked diphenyl branches on both sides. Electronic absorption spectra were stimulated using the semi-empirical TD method (for singlets only). Table 1**Error! Reference source not found.** contains the parameters of first and second excited electronic states ($S_0 \rightarrow S_1$ and $S_0 \rightarrow S_2$), both partially allowed with oscillator strength exceeding 0.2 and 0.5, respectively. Distributions of electron density for the HOMO and HOMO-1 as well as the LUMO and LUMO+1 for the **HTM1**–**HTM3** structures are presented in Figures S03, S04, S05, respectively.

Table 1. Electronic absorption spectra, simulated by Gaussian09 software, semi-empirical TD routine (for singlets only). Population of two lowest excited states.

	$S_0 \rightarrow S_1$		$S_0 \rightarrow S_2$	
	Transition energy, eV	Osc. Strength	Transition energy, eV	Osc. Strength

HTM 1	3.09	0.19	3.27	0.46
HTM 2	3.07	0.21	3.24	0.49
HTM 3	3.07	0.21	3.25	0.54

For **HTM1**, the singlet S1 electronic state could be populated by means of two one-particle transitions, HOMO-1→LUMO and HOMO→LUMO, favouring charge delocalization in the left fragment (more chaotic). In this case, the TB fragment plays an important role as a bridge fragment, containing two nitrogen atoms, built-up from two related sextagons consisting of carbons, and nitrogens, connected by a one-valence junction. Due to the spatial orientation of sextagons having ~105° angle, a π-conjugated system occurs along the entire molecule, from the left to the right fragment. All three materials demonstrate weak blue-green fluorescence in THF solutions, peaking at ~500 nm (Table 2, Figure S09).

Figure 2 represents a typical charge redistribution process by populating the first excited electronic state S_1. The first and second central nitrogen atoms from TB are associated to the π-conjugated systems, expanded by enamine-linked diphenyl branches, on the left and right sides, respectively. A separation line goes through the central structural peak represented by the –CH_2– group, connecting two nitrogen atoms. Due to a nonstandard off-plane angle of fragment orientation (105°), a π-conjugated system occurs along the molecule. From classical molecular electronics perspective, TB acts as a switch (HOMO distribution corresponds to switch-on, LUMO – switch-off). After excitation, charge localization is limited by a nitrogen in the right enamine-linked fragment, indicating the establishment of a radical cation [24]. For **HTM2** and **HTM3**, their charge redistribution properties are less expressed, but the common tendencies remain. Therefore, it is possible to assume that additional fragments such as methyl or methoxy groups increase the chaoticity within the enamine-linked diphenyl branches to shorten the length of conjugation within them.

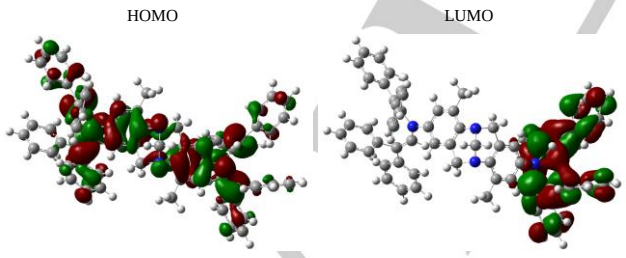

Figure 2. HTM1 structure, XZ projection. Role of TB (in center) in charge redistribution processes by populating the first excited electronic state S1.

Thermogravimetric analysis (TGA) of **HTM1** and **HTM3** confirms high thermal stability up to ~400 °C. Only **HTM2** started to decompose at the lower temperature of ~315 °C (Figure 3, Table 2). Thermal stability in the presence of dopants was also investigated (Figure S08), suggesting evaporation of the residual solvent and *tert*-butylpyridine at lower temperatures, with significant weight loss starting above ~290–300 °C. This indicates somewhat reduced but still sufficient thermal stability. Besides, differential scanning calorimetry (DSC) revealed that **HTM1** and **HTM3** exist both in crystalline and amorphous states (Table 2 and Figure S07), while no melting in derivative **HTM2** was detected (Figure 3). No crystallization was observed during cooling or second heating scans. Only a glass transition (T_g) of **HTM1**–**HTM3** was registered during the second heating (Figure 4), which is desirable for the formation of uniform films. The coexistence of these two states could be explained as crystallization is often observed in enamine compounds, while the amorphousness of compound is influenced by the non-planar structure of the TB core and structural bulk added by diphenylethenyl moieties. Compound **HTM2** is amorphous presumably due to the methyl groups on each of terminal phenyl rings. Note that a high glass transition temperature of **HTM3**, reaching 176 °C compared to 126 °C for Spiro-OMeTAD, can potentially facilitate device applications.

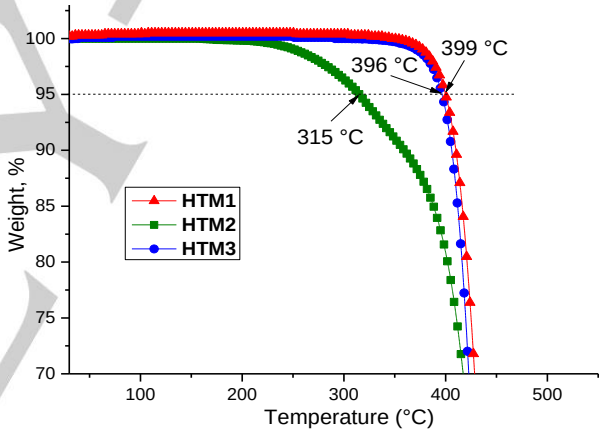

Figure 3. TGA curves for **HTM1**–**HTM3**.

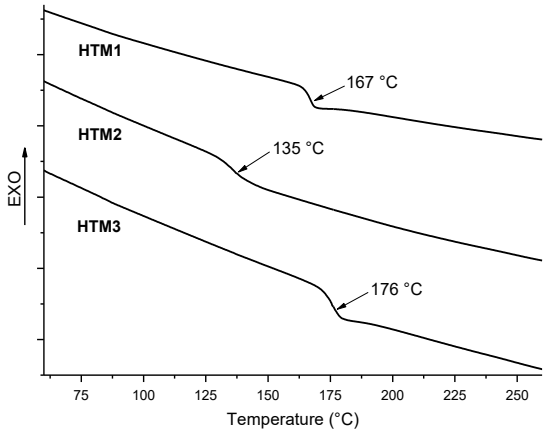

Figure 4. DSC curves for the second run of **HTM1**–**HTM3** at a T_g, heating rate 10 K/min.

The UV-VIS absorption bands of **HTM1**–**HTM3**, measured in THF (c = 10^{-4} mol/l, d = 1 mm) (Figure 5), indicate relevant bathochromic and hyperchromic shifts compared to the starting diamino compound **2**. Such a difference corresponds to the expansion of the π-conjugated system achieved by the enamine linking the diphenylethenyl branches. Differences between compounds **HTM1**–**HTM3** are also noticeable (despite the aromatic part being essentially the same in all three), i.e. the *p*-substituents of the terminal phenyl rings in **HTM1**, **HTM2**, and **HTM3** (none, methyl and methoxy, respectively) causes slight bathochromic (~1 nm differences) and hyperchromic shifts. The case of **HTM3** is particularly interesting as the absorption intensity in the range 240-290 nm increases, having maximum value at 261 nm, which might correspond to *n*-σ^* electron transitions in the proximity of oxygen atoms in methoxy substituents.

Table 2. Thermal and optical properties of **HTM1**–**HTM3**.

	T_m [°C] [a]	T_g [°C] [b]	T_{dec} [°C] [c]	λ_{max}^{abs} [nm] [d]	ε [$M^{-1}cm^{-1}$]	λ_{max}^{FL} [nm] [e]
HTM1	363	167	399	341	53000	501
HTM2	-	135	315	342	54850	502
HTM3	229	176	396	261; 343	69200; 56000	507
spiro[15]	245	126	449	387	69000	–

[a] Melting point during the first heating: heating rate 10 K/min. [b] Determined by DSC: scan rate 10 K/min; N_2 atmosphere; second run. [c] Onset of decomposition determined by TGA: heating rate 10 K/min; N_2 atmosphere. [d] In 10^{-4} M THF solution. [e] In 10^{-5} M THF solution, λ_{ex}=350 nm.

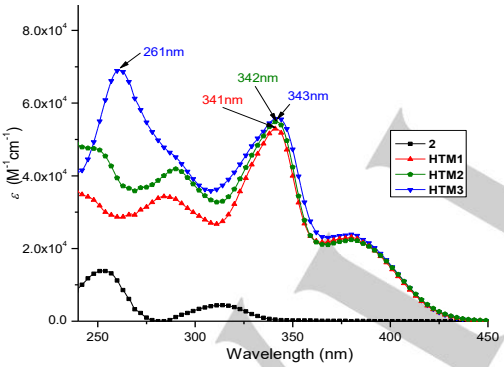

Figure 5. Absorption spectra of 1×10^{-4} M THF solutions of compounds **HTM1**–**HTM3** and **2** for comparison.

To have a better understanding of the HTM energy levels, their redox properties were determined by cyclic voltammetry (CV) performed in dry dichloromethane, containing 0.1 M tetrabutylammonium hexafluorophosphate (Table 3). The HOMO values are estimated to be -5.31, -5.17 and -5.11 eV for **HTM1**, **HTM2** and **HTM3** (Figure S06), respectively, suggesting feasible hole injection from the perovskite. The solid-state ionization potentials (I_p) were measured by photoelectron spectroscopy in air (PESA). According to this data (Figure 6), I_p of **HTM1** reaches a value of 5.54 eV making its use in PSCs doubtful. Electron donating methyl and methoxy groups attached to terminal phenyl rings lower I_p by 0.1 eV and 0.29 eV, respectively, resulting in 5.44 eV for **HTM2** and 5.25 eV for **HTM3**. Note that values in the solid state differ more significantly than the ones obtained in solution, probably due to different solid-state molecular packing.

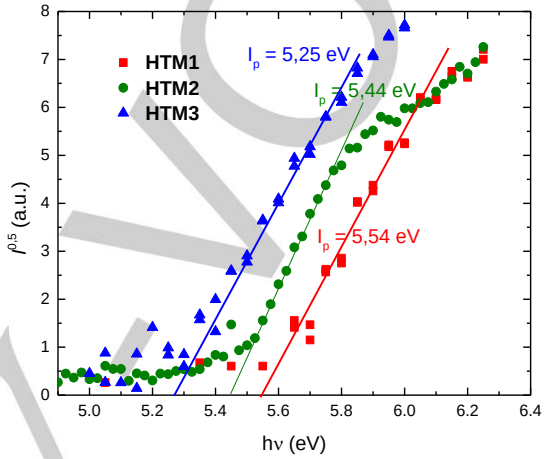

Figure 6. Photoemission in air spectra of **HTM1**–**HTM3**.

Table 3. Energy levels and hole mobility data for **HTM1**–**HTM3** and Spiro-OMeTAD for comparison.[a]

Compound	E_g^{opt} (eV)[b]	E_{HOMO} (eV)[c]	E_{LUMO} (eV)[d]	I_p, eV[e]	μ_0, cm^2/Vs[f]	μ (6.4×10^5 V/cm), cm^2/Vs[g]
HTM1	2.80	-5.31	-2.51	5.54	-[h]	-[h]
HTM2	2.80	-5.17	-2.37	5.44	- 4.0×10^{-6} [i]	~2×10^{-3} 1.5×10^{-5} [i]
HTM3	2.80	-5.11	-2.31	5.25	2.1×10^{-5} 1.4×10^{-6}	7.4×10^{-4} 7.6×10^{-6}
Spiro-OMeTAD	3.01	-5.12 [23]	-2.11	5.22 [30]	1.2×10^{-4}; 2.9×10^{-6} [i]	5.2×10^{-3}; 3.6×10^{-5} [i]

[a]CV measurements carried out with a glassy carbon electrode in dichloromethane containing 0.1 M tetrabutylammonium hexafluorophosphate with a Pt wire reference electrode. Potentials measured vs Fc^+/Fc. [b]Optical band gaps E_g^{opt} estimated from the edges of electronic absorption spectra. [c]Conversion factors: Fc in DCM vs SCE 0.46[31],SCE vs SHE: 0.244[32], SHE vs. vacuum: 4.43[33]. [d]E_{LUMO} calculated from the equation $E_{LUMO} = E_{HOMO} - E_g^{otp}$. [e]Solid state ionization potential (I_p) measured by photoemission in air from films. [f]Mobility value at zero field strength. [g]Mobility value at 6.4×10^5 V cm^{-1} field strength. [h]Film suitable for XTOF measurements were not obtained. [i]Mobility values were measured from the mixture of compound and PC-Z (1:1).

We also analyzed the charge transport properties of **HTM1**–**HTM3** and Spiro-OMeTAD by using the xerographic time of flight (XTOF) technique (Figure 7). Films of the molecules with bisphenol-Z polycarbonate (PC-Z) were fabricated and dependence of hole drift mobility on electric field strength was

measured. The values of charge mobility defining parameters, zero field mobility (μ_0), and the mobility at the electric field of 6.4×10^5 V cm^{-1}, are given in the Table 3. As electric fields are weak in the devices, charge mobility values near 0 V cm^{-1} field strength are more relevant, being the hole-drift mobility of **HTM3** $2.1\cdot10^{-5}$ cm^2 V^{-1} s^{-1}, one order of magnitude lower compared to Spiro-OMeTAD. To improve film quality of **HTM1** and **HTM2** (Figure S16) we employed a mixture of HTM and PC-Z in a 1:1 ratio (by weight), yet the quality of **HTM1 layer** (Figure S17) was not sufficient (Figure S18a and S18c). However, despite charge mobility will be lower compared with neat films, it is possible to compare materials measured under equal conditions. Thus, hole-drift mobilities of $4.0\cdot10^{-6}$ cm^2 V^{-1} s^{-1} (for **HTM2**+PC) and $1.4\cdot10^{-6}$ cm^2 V^{-1} s^{-1} (for **HTM3**+PC) at weak electric fields were estimated to be comparable to Spiro-OMeTAD+PC.

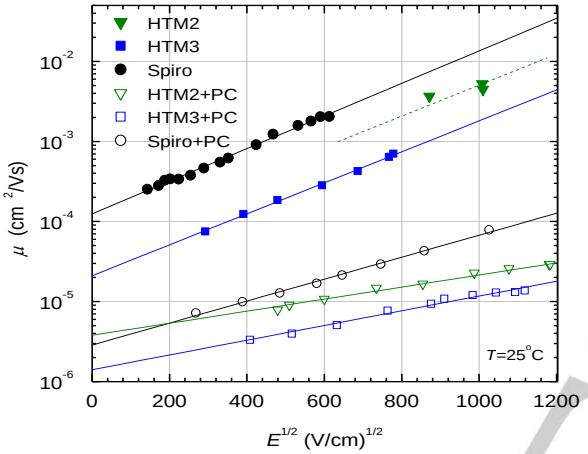

Figure 7. Electric field dependencies of the hole drift mobilities (μ) in the charge-transport layers of **HTM2**, **HTM3** and Spiro-OMeTAD.

Finally, **HTM1**–**HTM3** were applied as HTMs in PSCs. In brief, the devices had an optimized architecture based on FTO/ TiO_2 blocking / mesoporous TiO_2 / amorphous SnO_2 / perovskite / HTM/ Au [34]. A cross-sectional scanning electron microscopy (SEM) image from a complete device is presented in Figure 8a. This image confirms a perovskite film with around 600 nm thickness infiltrated in a 200 nm mesoporous TiO_2 layer, and approximately 30 nm of HTM homogeneously distributed on top. We employed a mixed perovskite composition containing $[(FAPbI_3)_{0.87}(MAPbBr_3)_{0.13}]_{0.92}(CsPbI_3)_{0.08}$, consisting on a multi-crystalline film with grain-crystals of ~ 200 nm (Figure 8b). The image for a typical perovskite/HTM layer stack is also included.

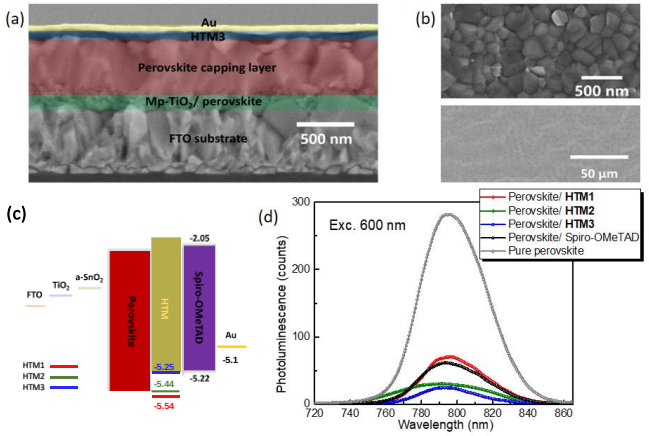

Figure 8. a) Cross-sectional SEM image a typical PSC containing **HTM3**. b) Surface SEM image of the perovskite *(top)* and perovskite/**HTM3** films *(bottom)*. c) Energy band diagrams of the device architecture. d) Steady-state PL spectra of the perovskite films covered with the studied HTMs.

The energy levels of the materials (Figure 8c) show a suitable ionization potential for **HTM3** (5.25 eV), close to that observed for Spiro-OMeTAD (5.22 eV) [30], facilitating the hole injection from the perovskite (5.40 eV) [35], whereas I_p of **HTM1** (5.54 eV) and **HTM2** (5.44 eV) are less favorable. Steady-state photoluminescence (PL) measurements under excitation of 600 nm (Figure 8d) revealed a quenching effect in the presence of the HTMs [36]. The intensity of the quenched emission followed the order of **HTM1** > Spiro-OMeTAD > **HTM2** > **HTM3**, suggesting **HTM3** as the best extraction layer [37].

J-V measurements for the cells containing the HTMs were performed under two different conditions: in the presence and absence of chemical dopants like *tert*-butylpyridine (TBP), tris(2-(1*H*-pyrazol-1-yl)-4-*tert*-butylpyridine) cobalt(III) (FK209) solution, and tris(bis(trifluoromethylsulfon-yl)imide) (Li-TFSI)). The *J-V* curves obtained for **HTM1**–**HTM3** in both cases are presented in Figure S19 and Table S2. Notably, cells containing **HTM1** and **HTM3** performed considerably better than Spiro-OMeTAD under dopant-free conditions, showing enhanced short-circuit current (J_{sc}) and fill factor (*FF*). Yet the V_{oc} remained relatively low in all cases, below 1.0 V. Interestingly, dopant-free **HTM3** exhibited a high J_{SC} over 23 mA·cm^{-2} and a PCE over 14%. In contrast, cells with doped **HTM3** and Spiro-OMeTAD were remarkably improved, with **HTM3** exhibiting an average efficiency of 18.14% and a record value of 18.62%. **HTM1** and **HTM2** resulted in very low efficiencies, probably due to the unsuitable match on their HOMO energy levels. The methoxy groups in **HTM3** not only favorably adjusts the energy levels, but also anchors the material onto the perovskite layer, thus resulting in more efficient hole injection [38,39]. Table 4 summarizes the impact of dopants in both systems.

Table 4. Device parameters extracted from *J-V* curves.

	HTMs	J_{sc} (mA/cm^2)	V_{oc} (mV)	*FF* (%)	PCE (%)
With Dopants	Spiro-OMeTAD	23.37	1045	78.7	19.22
	HTM3	23.31	1042	76.7	**18.62**

Dopant	Spiro-OMeTAD	21.73	795	51.7	8.92
free	**HTM3**	23.05	984	62.7	**14.23**

The *J-V* curves obtained for the champion cells based on **HTM3** and Spiro-OMeTAD are summarized in Figure 9 (see also Figure S20). The graph includes the values measured under forward and reverse bias, demonstrating a very limited hysteresis below 3% (PCE_{Rsc} = 18.62%, J_{Rsc}=23.31 mA/cm^2, V_{Roc}=1042 mV, and FF_R=0.767; PCE_{Fsc}= 18.12%; J_{Rsc}=23.21 mA/cm^2, V_{Roc}=1038 mV, and FF_R=0.752) (further tests exploring the influence of the HTM thickness were also performed, see Figure S21, with 20mM resulting the optimal condition, also employed for the other HTMs). In addition, the incident photon-to-current conversion (IPCE) shown in Figure 9b demonstrates a very high current generation over whole range of the visible spectra, leading to values close to 90% in the region 400 to 850 nm. These spectra results in an integrated photocurrent of 23.12 and 23.20 mA/cm^2 for **HTM3** and Spiro-OMeTAD respectively, in full agreement with the J_{sc} values.

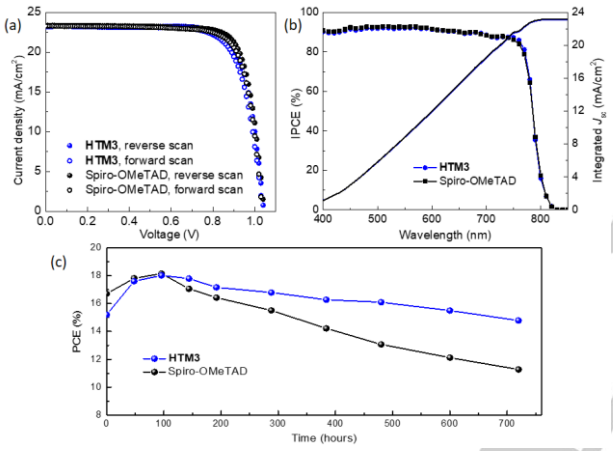

Figure 9. a) Forward and reverse scans of the champion cells using **HTM3** and spiro-OMeTAD (100 mV s^{-1}). b) IPCE spectra of devices based on **HTM3** and spiro-OMeTAD. c) Stability of non-encapsulated cells kept in ambient air (relative humidity ~50%, dark).

Finally, we further evaluated the stability of the record devices prepared with **HTM3** and Spiro-OMeTAD. The devices, stored in air with a relative humidity of ~50% (cells non-encapsulated), were measured under 100 mW/cm^2 simulated sun irradiation (1.5 AM). The results (Figure 9c) demonstrate enhanced PCE for both systems after the first 100 hours, but a remarkable difference after prolong-time periods. Interestingly, **HTM3** maintains >90% of the initial efficiency after tracking the cells during 700 h, whereas Spiro-OMeTAD drops to 65%. Cells containing **HTM3** without incorporating dopants were also evaluated, showing a remarkable stability in the first 300 h of evaluation (see Figure S22).

In conclusion, the synthesis of three novel enamine derivatives based on TB scaffold was described. These compounds were obtained in a facile three-step synthesis from simple, commercially available materials, without requiring expensive palladium catalysts or inert reaction conditions. **HTM1** and **HTM2** were purified via crystallization, hence eliminating the need of column chromatography or purification through sublimation. All materials were comprehensively characterized and device-tested in perovskite solar cells. The best performing material, **HTM3**, demonstrated 18.62% PCE, thus rivaling Spiro-OMeTAD in efficiency, while showing superior stability in non-encapsulated PSCs. Due to their suitable properties and convenient synthesis, these materials can potentially find uses in other optoelectronic applications.

Acknowledgements

The authors acknowledge funding from the European Union`s Horizon 2020 research and innovation programme under grant agreement No. 763977 of the PerTPV project and Research Council of Lithuania (grant No. MIP-17-70), and E. Kamarauskas for measurements of ionization potential. Computations were performed on resources at the High Performance Computing Center „HPC Saulėtekis“ (Faculty of Physics, Vilnius University). C. Momblona thanks to the co-funded Marie Skłodowska Curie fellowship H2020 grant agreement No 754462.

Keywords: Hole transporting material • Perovskite • Tröger's Base Scaffold • Enamines

[1] H. J. Snaith, *Nat. Mater.*, **2018**, 17, 372.
[2] M. A. Green and A. Ho-Baillie, *ACS Energy Lett.*, **2017**, 2, 822–830.
[3] N. J. Jeon, H. Na, E. H. Jung, T.-Y. Yang, Y. G. Lee, G. Kim, H.-W. Shin, S. Il Seok, J. Lee and J. Seo, *Nat. Energy*, **2018**, 3, 682–689.
[4] H.-S. Kim, C.-R. Lee, J.-H. Im, K.-B. Lee, T. Moehl, A. Marchioro, S.-J. Moon, R. Humphry-Baker, J.-H. Yum and J. E. Moser, *Sci. Rep.*, **2012**, 2, 591.
[5] N.-G. Park, *J. Phys. Chem. Lett.*, **2013**, 4, 2423–2429.
[6] S. Park, J. H. Heo, C. H. Cheon, H. Kim, S. H. Im and H. J. Son, *J. Mater. Chem. A*, **2015**, 3, 24215–24220.
[7] O. Malinkiewicz, A. Yella, Y. H. Lee, G. M. Espallargas, M. Graetzel, M. K. Nazeeruddin and H. J. Bolink, *Nat. Photonics*, **2014**, 8, 128.
[8] S. Kazim, M. K. Nazeeruddin, M. Grätzel and S. Ahmad, *Angew. Chemie Int. Ed.*, **2014**, 53, 2812–2824.
[9] J. Burschka, A. Dualeh, F. Kessler, E. Baranoff, N.-L. Cevey-Ha, C. Yi, M. K. Nazeeruddin and M. Grätzel, *J. Am. Chem. Soc.*, **2011**, 133, 18042–18045.
[10] S. D. Stranks, G. E. Eperon, G. Grancini, C. Menelaou, M. J. P. Alcocer, T. Leijtens, L. M. Herz, A. Petrozza and H. J. Snaith, *Science*, **2013**, 342, 341–344.
[11] G. Xing, N. Mathews, S. Sun, S. S. Lim, Y. M. Lam, M. Grätzel, S. Mhaisalkar and T. C. Sum, *Science*, **2013**, 342, 344–347.
[12] Z. Yu and L. Sun, *Adv. Energy Mater.*, **2015**, 5, 1500213.
[13] H. Kim, K.-G. Lim and T.-W. Lee, *Energy Environ. Sci.*, **2016**, 9, 12–30.
[14] A. Binek, M. L. Petrus, N. Huber, H. Bristow, Y. Hu, T. Bein and P. Docampo, *ACS Appl. Mater. Interfaces*, **2016**, 8, 12881–12886.
[15] T. Malinauskas, M. Saliba, T. Matsui, M. Daskeviciene, S. Urnikaite, P. Gratia, R. Send, H. Wonneberger, I. Bruder and M. Graetzel, *Energy Environ. Sci.*, **2016**, 9, 1681–1686.
[16] K. Rakstys, M. Saliba, P. Gao, P. Gratia, E. Kamarauskas, S. Paek, V. Jankauskas and M. K. Nazeeruddin, *Angew. Chemie*, **2016**, 128, 7590–7594.
[17] M. Maciejczyk, A. Ivaturi and N. Robertson, *J. Mater. Chem. A*, **2016**, 4, 4855–4863.
[18] B. Xu, D. Bi, Y. Hua, P. Liu, M. Cheng, M. Grätzel, L. Kloo, A. Hagfeldt and L. Sun, *Energy Environ. Sci.*, **2016**, 9, 873–877.

[19] D. Bi, B. Xu, P. Gao, L. Sun, M. Graetzel and A. Hagfeldt, *Nano Energy*, **2016**, 23, 138–144.

[20] P. Gratia, A. Magomedov, T. Malinauskas, M. Daskeviciene, A. Abate, S. Ahmad, M. Grätzel, V. Getautis and M. K. Nazeeruddin, *Angew. Chemie Int. Ed.*, **2015**, 54, 11409–11413.

[21] A. Magomedov, N. Sakai, E. Kamarauskas, G. Jokubauskaitė, M. Franckevičius, V. Jankauskas, H. J. Snaith and V. Getautis, *Chem. Asian J.*, **2017**, 12, 958–962.

[22] Š. Daškevičiūtė, N. Sakai, M. Franckevičius, M. Daškevičienė, A. Magomedov, V. Jankauskas, H. J. Snaith and V. Getautis, *Adv. Sci.*, **2018**, 5, 1700811.

[23] M. Daskeviciene, S. Paek, Z. Wang, T. Malinauskas, G. Jokubauskaite, K. Rakstys, K. T. Cho, A. Magomedov, V. Jankauskas, S. Ahmad, H. J. Snaith, V. Getautis and M. K. Nazeeruddin, *Nano Energy*, **2017**, 32, 551–557.

[24] C. L. Ramírez, C. Pegoraro, L. Trupp, A. Bruttomesso, V. Amorebieta, D. M. A. Vera and A. R. Parise, *Phys. Chem. Chem. Phys.*, **2011**, 13, 20076.

[25] T. P. Osedach, T. L. Andrew, V. Bulovic, *Energy Environ. Sci.* **2013**, *6*, 711.

[26] M. L. Petrus, T. Bein, T. J. Dingemans, P. Docampo, *J. Mater. Chem. A* **2015**, *3*, 12159.

[27] M. Degbia, M. Ben Manaa, B. Schmaltz, N. Berton, J. Boucle, R. Antony, F. Tran Van, Mater., Sci. Semicond. Process. 43 (2016) 90–95.

[28] O. Usluer, M. Cloutet, G. Hadziioannou, ACS Macro Lett. 3 (2014) 1134–1138.

[29] M. J. Frisch, G. W. Trucks, H. B. Schlegel, G. E. Scuseria, M. A. Robb, J. R. Cheeseman, G. Scalmani, V. Barone, B. Mennucci, G. A. Petersson, H. Nakatsuji, M. Caricato, X. Li, H. P. Hratchian, A. F. Izmaylov, J. Bloino, G. Zheng, J. L. Sonnenberg, M. Hada, M. Ehara, K. Toyota, R. Fukuda, J. Hasegawa, M. Ishida, T. Nakajima, Y. Honda, O. Kitao, H. Nakai, T. Vreven, J. A. Montgomery Jr., J. E. Peralta, F. Ogliaro, M. Bearpark, J. J. Heyd, E. Brothers, K. N. Kudin, V. N. Staroverov, T. Keith, R. Kobayashi, J. Normand, K. Raghavachari, A. Rendell, J. C. Burant, S. S. Iyengar, J. Tomasi, M. Cossi, N. Rega, J. M. Millam, M. Klene, J. E. Knox, J. B. Cross, V. Bakken, C. Adamo, J. Jaramillo, R. Gomperts, R. E. Stratmann, O. Yazyev, A. J. Austin, R. Cammi, C. Pomelli, J. W. Ochterski, R. L. Martin, K. Morokuma, V. G. Zakrzewski, G. A. Voth, P. Salvador, J. J. Dannenberg, S. Dapprich, A. D. Daniels, O. Farkas, J. B. Foresman, J. V. Ortiz, J. Cioslowski and D. J. Fox, *Gaussian Inc. Wallingford, CT, USA*, **2013**.

[30] K. T. Cho, O. Trukhina, C. Roldán-Carmona, M. Ince, P. Gratia, G. Grancini, P. Gao, T. Marszalek, W. Pisula and P. Y. Reddy, *Adv. Energy Mater.*, **2017**, 7, 1601733.

[31] N. G. Connelly and W. E. Geiger, *Chem. Rev.*, **1996**, 96, 877–910.

[32] V. V Pavlishchuk and A. W. Addison, *Inorganica Chim. Acta*, **2000**, 298, 97–102.

[33] H. Reiss and A. Heller, *J. Phys. Chem.*, **1985**, 89, 4207–4213.

[34] M. M. Tavakoli, F. Giordano, S. M. Zakeeruddin and M. Grätzel, *Nano Lett.*, **2018**, 18, 2428–2434.

[35] M. Salado, R. K. Kokal, L. Calio, S. Kazim, M. Deepa, S. Ahmad, *Phys. Chem. Chem. Phys.*, **2017**, 19, 22905–22914.

[36] I. Zimmermann, J. Urieta-Mora, P. Gratia, J. Aragó, G. Grancini, A. Molina-Ontoria, E. Ortí, N. Martín and M. K. Nazeeruddin, *Adv. Energy Mater.*, **2017**, 7, 1601674.

[37] S. Paek, P. Qin, Y. Lee, K. T. Cho, P. Gao, G. Grancini, E. Oveisi, P. Gratia, K. Rakstys and S. A. Al-Muhtaseb, *Adv. Mater.*, **2017**, 29, 1606555.

[38] P. Schulz, D. Cahen, A. Kahn, *Chem. Rev.*, **2019**, 119, 3349–3417.

[39] L. Calió, S. Kazim, M. Grätzel, S. Ahmad, *Angew. Chem. Int. Ed.* **2016**, 55, 14522–14545.

Entry for the Table of Contents

COMMUNICATION

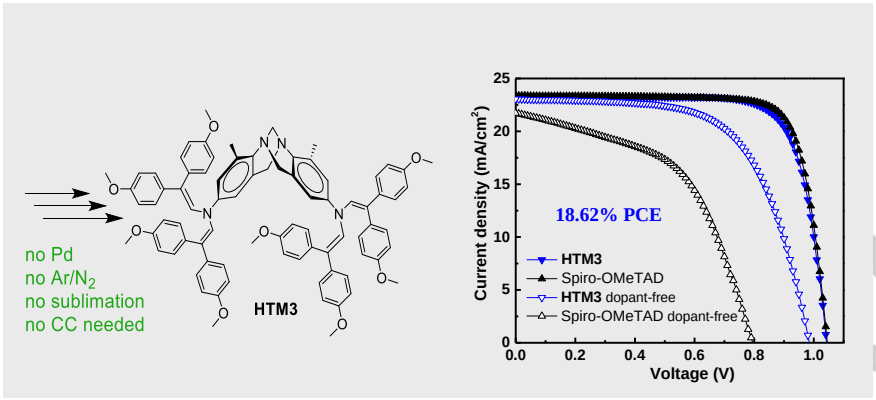

Titas Braukyla,[†][a] Rui Xia,[†][b] Maryte Daskeviciene,[a] Tadas Malinauskas,[a] Alytis Gruodis,[c] Vygintas Jankauskas,[c] Paul Dyson,[d] Cristina Momblona,[b] Cristina Roldán-Carmona,[b] Vytautas Getautis,[*][a] Mohammad Khaja Nazeeruddin[*][b]

Page 1 – Page 8

Hole Transporting Enamines Based on Tröger's Base Scaffold for